Optics Letters

Eigenvalue calibration method for dual rotating-compensator Mueller matrix polarimetry

Sheng Sheng, Xiuguo Chen,* Chao Chen, Jinfeng Zhuang, Cai Wang, Honggang Gu, and Shiyuan Liu

State Key Laboratory of Digital Manufacturing Equipment and Technology, Huazhong University Science and Technology, Wuhan 430074, China
**Corresponding author: xiuguochen@hust.edu.cn*

Received 12 July 2021; revised 6 August 2021; accepted 6 August 2021; posted 13 August 2021 (Doc. ID 437542); published 13 September 2021

Dual rotating-compensator Mueller matrix polarimetry (DRC-MMP) has achieved wide spread applications in material characterization, nano-scale measurement, and biomedical diagnostics. However, the traditional calibration method for DRC-MMP relies on establishing an accurate system model, making its implementation cumbersome, especially in the presence of polarizing components that are to complex to be modeled. We propose a novel, to the best of our knowledge, eigenvalue calibration method for DRC-MMP without system modeling. Two specific basis vectors are introduced in order to transform the continuously modulated light intensity in DRC-MMP into a 5 × 5 projection matrix. Eigenvalue analysis is then performed based on the light intensity projection matrix to obtain the modulation matrix and the analysis matrix associated with the polarization state generator and the polarization state analyzer, respectively. The method is applied for DRC-MMP in both single-pass and double-pass setups. The experimental results have verified the proposed calibration method.

https://doi.org/10.1364/OL.437542

Mueller matrix polarimetry (MMP) has shown great potential in material characterization [1], nano-scale measurement [2], and biomedical diagnositics [3], due to its advantages of noncontactness, noninvasion, and more comprehensive information. Compared with other types of MMPs, such as the MMP based on liquid crystals [4], the dual rotating-compensator MMP (DRC-MMP) [5] can realize broader spectral measurements and has a higher temperature stability, thus achieving a wider range of applications.

To achieve accurate measurements, delicate calibration needs to be performed in advance. As illustrated in Section 1 of Supplement 1, the traditional calibration method for DRC-MMP, termed as the model-based calibration method (MCM), relies on establishing a system model [5,6]. The established system model should take all the optical components that change polarization states into account, making the implementation of MCM in practice cumbersome, especially in the presence of beam splitters and high numerical aperture objective lenses [7].

As opposed to MCM, a model-free method, i.e., the eigenvalue calibration method (ECM) [8], is commonly adopted in MMP based on liquid crystals by measuring a series of calibration samples. Then transforming the calibration into eigenvalues and eigenvectors of a linear system of equations. It is noted that so far, that ECM is typically used for well-determined linear systems whose number of measured fluxes is equal to that of the Mueller matrix elements [9,10]. However, in DRC-MMP, the number of measured fluxes is much greater than that of the Mueller matrix elements. To the best of our knowledge, ECM has never been used in over-determined linear systems. Although several works have reported the application of ECM to the calibration of DRC-MMP [11], it is noted that the two compensators in DRC-MMP did not rotate continuously to transform the calibration to a well-determined calculation procedure.

In this Letter, we propose a novel ECM for DRC-MMP. We introduce two specific basis vectors and then project the collected light intensity into the above basis vectors. The projection process transforms the continuously modulated light intensity into a 5 × 5 projection matrix. The traditional ECM is then extended to the 5 × 5 light intensity projection matrix. Details of the proposed ECM have been presented for DRC-MMP in both single and double-pass setups. The experimental results have verified the proposed method.

Figure 1 summarizes the common setups for DRC-MMP. The polarization state generator (PSG) composed of a polarizer (P) and a compensator (C1) modulates the polarization state of the incident light, and the polarization state analyzer (PSA) composed of a compensator (C2) and an analyzer (A) demodulates the polarization state of the emitted light. The two compensators rotate at a fixed speed ratio. The typical system parameters under calibration include the orientations of the transmission axes of the polarizer and analyzer, θ_P and θ_A, the orientations of the fast axes of the two compensators, θ_{C1} and θ_{C2}, as well as the retardances of the two compensators, δ_{C1} and δ_{C2}.

For DRC-MMP, the light intensity $I(t)$ collected by the detector can be generally expressed as

$$\begin{aligned} I(t) &= [1, 0, 0, 0] \cdot \mathbf{M}_{\mathrm{PSA}}(t) \cdot \mathbf{M}_S \cdot \mathbf{M}_{\mathrm{PSG}}(t) \cdot \mathbf{S}_{\mathrm{in}} \\ &= A_{\mathrm{PSA}}^T(t) \cdot \mathbf{M}_S \cdot S_{\mathrm{PSG}}(t), \end{aligned} \tag{1}$$

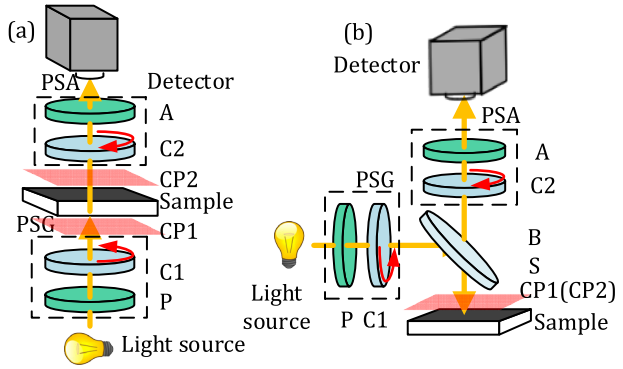

Fig. 1. Schematic diagram for DRC-MMP in (a) a single-pass setup and (b) a double-pass setup. BS, beam splitter, CP1,2, the calibration planes.

where $\mathbf{S}_{\text{in}}$ denotes the Stokes vector of the incident light, $\mathbf{M}_S$ is the Mueller matrix of the sample, and $\mathbf{M}_{\text{PSG}}(t)$ and $\mathbf{M}_{\text{PSA}}(t)$ correspond to the Mueller matrices of PSG and PSA, respectively. Due to the two continuously rotating compensators, $\mathbf{M}_{\text{PSG}}(t)$ and $\mathbf{M}_{\text{PSA}}(t)$ are both a function of time, and the collected light intensity $I(t)$ is a continuous temporal signal. The $\mathbf{S}_{\text{PSG}}(t)$ denotes the temporal Stokes vector generated by PSG, and $\mathbf{A}_{\text{PSA}}(t)$ is the corresponding temporal analyzer vector prepared by PSA.

Assuming that the rotary speed ratio of the two compensators is p: q, where p and q are integers, we choose the modulation basis vector $\Theta_{\mathbf{W}}(t)$ and the analysis basis vector $\Theta_{\mathbf{A}}(t)$ for PSG and PSA, respectively, which are given by

$$\Theta_{\mathbf{W}}(t) = \left[1, \cos 2p\omega t, \sin 2p\omega t, \cos 4p\omega t, \sin 4p\omega t\right]^T$$
$$\Theta_{\mathbf{A}}(t) = \left[1, \cos 2q\omega t, \sin 2q\omega t, \cos 4q\omega t, \sin 4q\omega t\right]^T, \tag{2}$$

where ω is the fundamental frequency. Projecting $\mathbf{S}_{\text{PSG}}(t)$ and $\mathbf{A}_{\text{PSA}}(t)$ onto the above basis vectors respectively, Eq. (1) is rewritten as

$$I(t) = \Theta_{\mathbf{A}}^T(t) \cdot \mathbf{A} \cdot \mathbf{M}_S \cdot \mathbf{W} \cdot \Theta_{\mathbf{W}}(t)$$
$$= \Theta_{\mathbf{A}}^T(t) \cdot \mathbf{D} \cdot \Theta_{\mathbf{W}}(t), \tag{3}$$

where the modulation matrix $\mathbf{W}$ and the analysis matrix $\mathbf{A}$ are the projection matrices of $\mathbf{S}_{\text{PSG}}(t)$ and $\mathbf{A}_{\text{PSA}}(t)$ onto $\Theta_{\mathbf{W}}(t)$) and $\Theta_{\mathbf{A}}(t)$, respectively, and $\mathbf{D} = \mathbf{A}\mathbf{M}_S\mathbf{W}$ is named the intensity projection matrix. The aim of the calibration is to obtain the modulation matrix $\mathbf{W}$ and the analysis matrix $\mathbf{A}$.

First, the null response of the system in the absence of the calibration samples is acquired, with the corresponding intensity projection matrix represented by

$$\mathbf{D}_0 = \mathbf{A}\mathbf{M}_0\mathbf{W}, \tag{4}$$

where $\mathbf{M}_0$ represents the Mueller matrix of air for the single-pass setup shown in Fig. 1(a) in the straight-through mode, or the Mueller matrix of any reflective sample with a non-singular Mueller matrix for the single-pass setup in the reflection mode and the double-pass setup shown in Fig. 1(b).

Next, a calibration measurement is performed by placing the calibration samples on the calibration plane CP1, as indicated in Fig. 1. Usually at least three calibration samples, such as polarizers and waveplates, are required for the calibration [8]. The acquired intensity projection matrix is denoted as

$$\mathbf{D}_{fi} = \mathbf{A}\mathbf{M}_{fi}\mathbf{W}. \tag{5}$$

In a similar manner, another calibration measurement is performed by placing the calibration samples on the calibration plane CP2. The acquired intensity projection matrix is denoted as

$$\mathbf{D}_{bi} = \mathbf{A}\mathbf{M}_{bi}\mathbf{W}. \tag{6}$$

For the single-pass system shown in Fig. 1(a), the Mueller matrices $\mathbf{M}_{fi}$ and $\mathbf{M}_{bi}$ are given by

$$\mathbf{M}_{fi} = \mathbf{M}_0 \cdot \mathbf{M}_i, \quad \mathbf{M}_{bi} = \mathbf{M}_i \cdot \mathbf{M}_0, \tag{7}$$

where $\mathbf{M}_i$ is the corresponding Mueller matrix of the ith ($i = 1, 2, 3, \ldots$) calibration sample. For the double-pass system shown in Fig. 1(b), we assume that the constituent materials of the calibration samples are reciprocal. Thereby, $\mathbf{M}_{fi}$ and $\mathbf{M}_{bi}$ are given by

$$\mathbf{M}_{fi} = \mathbf{M}_{bi} = \mathbf{M}_i \cdot \mathbf{M}_0 \cdot \mathbf{M}_i. \tag{8}$$

$\mathbf{A}$ is a column full-rank matrix, $\mathbf{W}$ is a row full-rank matrix, and the inverse of a non-square matrix is regarded as its Moore-Penrose pseudo-inverse matrix [12], denoted as

$$\mathbf{C}_{fi} = \mathbf{D}_0{}^{+}\mathbf{D}_{fi} = \mathbf{W}^{+}\mathbf{M}_0{}^{+}\mathbf{A}^{+}\mathbf{A}\mathbf{M}_{fi}\mathbf{W} = \mathbf{W}^{+}\mathbf{M}_0\mathbf{M}_{fi}\mathbf{W}$$
$$\mathbf{C}_{bi} = \mathbf{D}_{bi}\mathbf{D}_0{}^{+} = \mathbf{A}\mathbf{M}_{bi}\mathbf{W}\mathbf{W}^{+}\mathbf{M}_0{}^{+}\mathbf{A}^{+} = \mathbf{A}\mathbf{M}_{bi}\mathbf{M}_0\mathbf{A}^{+}. \tag{9}$$

It is found that $\mathbf{M}_{fi}$ ($\mathbf{M}_{bi}$) is a fourth order square matrix, while $\mathbf{C}_{fi}$ ($\mathbf{C}_{bi}$) is a fifth order square matrix. Combining Eq. (7), the relationship between the eigenvalues of $\mathbf{C}_{fi}$ ($\mathbf{C}_{bi}$) and the eigenvalues of $\mathbf{M}_{fi}$ ($\mathbf{M}_{bi}$) can be found and is another major difference from the traditional ECM. In the single-pass system, the non-zero eigenvalues of $\mathbf{C}_{fi}$ ($\mathbf{C}_{bi}$) are equal to the eigenvalues of $\mathbf{M}_{fi}$ ($\mathbf{M}_{bi}$), while in the double-pass system, the non-zero eigenvalues of $\mathbf{C}_{fi}$ ($\mathbf{C}_{bi}$) are the square of the eigenvalues of $\mathbf{M}_{fi}$ ($\mathbf{M}_{bi}$). Details of the relationship between the eigenvalues of $\mathbf{C}_{fi}$ ($\mathbf{C}_{bi}$) and $\mathbf{M}_{fi}$ ($\mathbf{M}_{bi}$) for the double-pass system can be found in Section 2 of Supplement 1. It can also be proven that the extra eigenvalue of $\mathbf{C}_{\text{fi}}$ ($\mathbf{C}_{\text{bi}}$) is 0 in the absence of error. So, intermediate matrices $\mathbf{T}_{fi}$ and $\mathbf{T}_{bi}$ can then be constructed as follows

$$\mathbf{T}_{fi} = \mathbf{M}_{fi}\mathbf{W} - \mathbf{W}\mathbf{D}_{fi}, \quad \mathbf{T}_{bi} = \mathbf{A}\mathbf{M}_{bi} - \mathbf{D}_{bi}\mathbf{A}. \tag{10}$$

Random noise is inevitably introduced into practical measurements, which will cause Eq. (10) to have no solution, so we choose the least square solution as the approximate solution of the equation. With the vectorization operator, Eq. (10) can be rewritten as

$$\text{vec}(\mathbf{T}_{fi}) = \text{vec}(\mathbf{M}_{fi}\mathbf{W} - \mathbf{W}\mathbf{C}_{fi}) = \mathbf{H}_{fi}\text{vec}(\mathbf{W})$$
$$\text{vec}(\mathbf{T}_{bi}) = \text{vec}(\mathbf{A}\mathbf{M}_{bi} - \mathbf{C}_{bi}\mathbf{A}) = \mathbf{H}_{bi}\text{vec}(\mathbf{A}). \tag{11}$$

To ensure that Eq. (11) is solvable, a positive semi-definite matrix needs to be constructed as follows

$$\left|\mathrm{vec}(\mathbf{T}_{fi})\right|^2 = \mathrm{vec}(\mathbf{W})^T\mathbf{H}_{fi}{}^T\mathbf{H}_{fi}\mathrm{vec}(\mathbf{W}) = \mathrm{vec}(\mathbf{W})^T\mathbf{K}_{fi}\mathrm{vec}(\mathbf{W})$$

$$|\mathrm{vec}(\mathbf{T}_{bi})|^2 = \mathrm{vec}(\mathbf{A})^T\mathbf{H}_{bi}{}^T\mathbf{H}_{bi}\mathrm{vec}(\mathbf{A}) = \mathrm{vec}(\mathbf{A})^T\mathbf{K}_{bi}\mathrm{vec}(\mathbf{A}). \tag{12}$$

$\mathrm{vec}(\mathbf{W})$ and $\mathrm{vec}(\mathbf{A})$ are the zero eigenvectors of $\mathbf{K}_{fi}$ and $\mathbf{K}_{bi}$, respectively. A more robust solution can be obtained by summing the results of multiple different calibration measurements as follows

$$\mathbf{K}_{\mathrm{tot}}\mathrm{vec}(\mathbf{W}) = 0, \quad \mathbf{K}'_{\mathrm{tot}}\mathrm{vec}(\mathbf{A}) = 0$$

$$\mathbf{K}_{\mathrm{tot}} = \sum_i \mathbf{K}_{fi}, \quad \mathbf{K}'_{\mathrm{tot}} = \sum_i \mathbf{K}_{bi}. \tag{13}$$

In theory, the selection of the calibration samples only needs to ensure that the sample is anisotropic, and its Mueller matrix is full rank, so that Eq. (12) has a unique solution.

Note that the positive semi-definite matrices $\mathbf{K}_{\mathrm{tot}}$ and $\mathbf{K}'_{\mathrm{tot}}$ have 20 eigenvalues, and their minimum and unique eigenvalue is 0. Assume that the 20 eigenvalues are denoted as $\lambda_1, \lambda_2, \lambda_3, \ldots, \lambda_{20}$ from large to small. Therefore, changing the azimuth angle of the Mueller matrix of the calibration sample in order to make $\lambda_{20}/\lambda_{19}$ take the minimum value the solution that minimizes the ratio is the true azimuth of the calibration samples. The zero eigenvectors can be rearranged to obtain the modulation matrix $\mathbf{W}$ and the analysis matrix $\mathbf{A}$ [8].

Verification of the intensity projection process: The light intensity projection process is a prerequisite for the above calibration procedure. The accuracy of the projection process is directly related to the calibration results of the modulation matrix $\mathbf{W}$ and the analysis matrix $\mathbf{A}$. In order to study the law of error propagation in the system, the signal projection process of a polarimeter with a rotary speed ratio of 5:3 shown in Fig. 1(a) was exemplified. The light intensity signal of the detector is a periodic function according to Eq. (1). The continuous light intensity signal can then be expressed in terms of Fourier series as follows

$$I(t) = I_0 + \sum_{n=1}^{16} (\alpha_{2n}\cos 2n\omega t + \beta_{2n}\sin 2n\omega t), \tag{14}$$

where ω is the fundamental frequency, I_0 is the direct-current component, and α_{2n} and β_{2n} are the Fourier coefficients. Substituting the rotary speed ratio of 5:3 into the basis vectors given in Eq. (2), and then rearranging Eq. (14) according to the form of Eq. (3), we can finally obtain the associated intensity projection matrix $\mathbf{D}$ as follows

$$\mathbf{D} = \begin{bmatrix} I_0 & \alpha_{10} & \beta_{10} & \alpha_{20} & \beta_{20} \\ \alpha_6 & \alpha_4+\alpha_{16} & \beta_4+\beta_{16} & \alpha_{14}+\alpha_{26} & \beta_{14}+\beta_{26} \\ \beta_6 & \beta_{16}-\beta_4 & \alpha_4-\alpha_{16} & \beta_{26}-\beta_{14} & \alpha_{14}-\alpha_{26} \\ \alpha_{12} & \alpha_2+\alpha_{22} & \beta_{22}-\beta_2 & \alpha_8+\alpha_{32} & \beta_8+\beta_{32} \\ \beta_{12} & \beta_2+\beta_{22} & \alpha_2-\alpha_{22} & \beta_{32}-\beta_8 & \alpha_8-\alpha_{32} \end{bmatrix}. \tag{15}$$

In the verification, two samples were simulated, including air and a polarizer. We then compared the theoretical and the reconstructed light intensities for the two samples. Here, the theoretical light intensities were obtained according to the system model as described in Eq. (1). The reconstructed light intensities were obtained according to Eq. (3) with the intensity projection matrix $\mathbf{D}$ given by Eq. (15). The aim of the comparison is to show that Eqs. (3) and (14) are mathematically equivalent. Figures 2(a) and 2(b) present the comparison results for air and the polarizer, respectively, where the theoretical intensity is denoted as a blue dashed line and the associated reconstructed intensity is denoted as a green line marked with filled circles. As can be seen from Fig. 2, the reconstructed light intensities agree well with the corresponding theoretical intensities for the two samples. It is therefore verified the correctness of the intensity projection process. In another word, the intensity projection matrix can be also used as another manifestation of the light intensity signal.

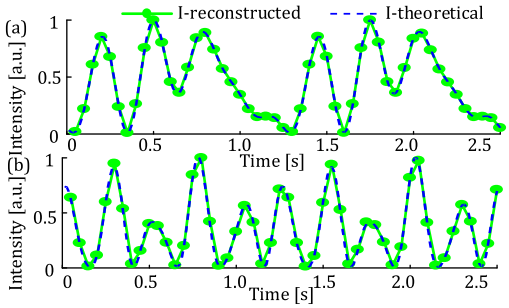

Fig. 2. Comparison between the theoretical and the reconstructed light intensities for samples: (a) air and (b) a polarizer, where the theoretical intensities were calculated by Eq. (1) and the reconstructed intensities were obtained by Eq. (3). The fundamental frequency $\omega = 0.8\pi$ Hz.

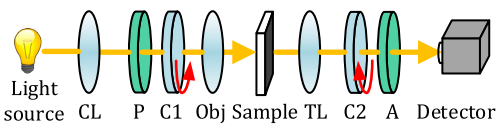

Fig. 3. Experimental setup for an imaging DRC-MMP. CL, collimator; P, polarizer; C1, first rotating compensator; Obj, objective lens; TL, tube lens; C2, second rotating compensator; A, analyzer.

Experiments: A DRC-MMP in the straight-through mode was set up to validate the ECM shown in Fig. 3. The light source was a high-intensity, high-stability, wide-spectrum white light source (LDLS EQ77, Energetic Technology) with a monochromator (CM100, Spectral Products). The PSG of this setup consisted of a linear polarizer (PGT5012, Union Optic) and a true zero-order quarter waveplate (@633 nm, Union Optic) driven by a hollow motor, the PSA also had the same structure, but the polarizer and waveplate were in opposite positions and the speed ratio of the two compensators was 5:3. In the imaging system, a chromogenic double glue lens (AC254-075-A-ML, Thorlabs) was used as an objective lens. The exposure time of the CCD camera (panda 4.0, PCO) was 47.97 ms. During the calibration process, four tests were completed in sequence. The calibration samples were air, a high-contrast glass linear polarizer (#47-316, Edmund Optics) with an azimuth angle of 0° and about 90°, and a polymer film quarter waveplate (WPQ05M-633, Thorlabs) with an azimuth angle of about 30°.

The MCM and ECM were adopted to calibrate the system. For the ECM, the calibration samples were measured separately and the modulation matrix $\mathbf{W}$ and the analysis matrix $\mathbf{A}$ can be calibrated with all the optical elements in the system considered including the objective lens Obj. Compared with ECM, the objective lens needs to be modeled first to take its polarization

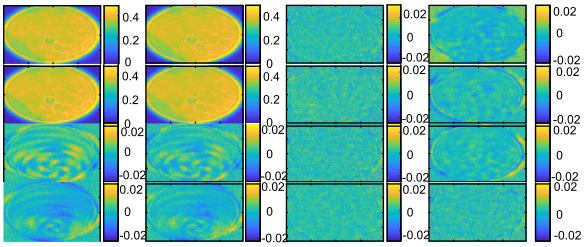

Fig. 4. Mueller matrix image of a polarizer obtained with the ECM calibration results.

effect into account in the calibration by MCM. However, considering that the numerical aperture of the employed objective lens here is no more than 0.3, we ignored its polarization effect in the calibration by MCM. The air was measured as a standard sample and a point at the center of the CCD was selected to calculate the Mueller matrix of air, and the results obtained by the two calibration methods are shown as

$$\mathbf{M}_{\mathrm{MCM}} = \begin{bmatrix} 1.000 & 0.0003 & -0.0007 & 0.0038 \\ 0.0007 & 0.9979 & 0.0029 & 0.0037 \\ -0.0003 & -0.0020 & 0.9987 & -0.0031 \\ 0.0038 & -0.0010 & -0.0015 & 0.9976 \end{bmatrix},$$

$$\mathbf{M}_{\mathrm{ECM}} = \begin{bmatrix} 1.000 & -0.0091 & 0.0057 & -0.0062 \\ -0.0095 & 0.9949 & -0.0098 & -0.0076 \\ 0.0030 & 0.0095 & 0.9985 & 0.0007 \\ -0.0035 & 0.0044 & -0.0054 & 0.9976 \end{bmatrix}. \quad \textbf{(16)}$$

As indicated in Eq. (16), the deviations of the two calibration methods are both no more than 0.01, and the errors in the calculated Mueller matrices are primarily attributed to random noise in the collected light intensities. Then, we measured and analyzed the Mueller matrix imaging results of a polarizer with a fingerprint stain, as shown in Fig. 4. In the Mueller matrix images of M_{31} and M_{32}, the outline of the fingerprint can be clearly seen, which cannot be observed in M_{11}. This shows the application potential in defect detection of optical materials.

In order to further demonstrate the advantages of ECM, these two methods were adapted to calibrate a more complex system shown in Fig. 1(b), where a non-polarizing beam splitter (BS) (BP145B1, Thorlabs) is installed between the PSG and the PSA. A reflection mirror (BB1-E02, Thorlabs) at normal incidence is used as a standard sample for testing. During the test, we adjust the light to irradiate the mirror vertically through the BS in the forward direction, then reflect vertically, pass through the BS in the reverse direction, and then reach the PSA, that is the double-pass setup.

For the MCM, the polarization effect of the BS was ignored to complete the system calibration, and then the Mueller matrix of the mirror was calculated. For the ECM, the polarization effect of the BS is automatically considered in the calibration. Detailed calibration procedure of the ECM for the double-pass setup is presented in Section 3 of the Supplement 1. The analysis results of the mirrors by the two methods are shown in Eq. (17).

According to Eq. (17), the deviations in $\mathbf{M}_{\mathrm{ECM}}$ do not exceed 0.01. However, the elements of the main diagonal block of $\mathbf{M}_{\mathrm{MCM}}$ have obvious deviations, especially for M_{34} and M_{43}, which is attributed to the residual polarization effect of the employed BS that is ignored in the implementation of MCM. After modeling the BS, the MCM results were greatly improved, as illustrated in Section 4 of the Supplement 1. However, since the modeling and calibration process of the BS is very cumbersome, the ECM, as a model-free calibration method, is very suitable for this complex ellipsometry system

$$\mathbf{M}_{\mathrm{MCM}} = \begin{bmatrix} 1.000 & 0.0979 & -0.0000 & -0.0041 \\ 0.0979 & 1.0000 & 0.0010 & 0.0004 \\ -0.0011 & 0.0007 & -0.9508 & 0.2938 \\ 0.0040 & 0.0011 & -0.2938 & -0.9508 \end{bmatrix},$$

$$\mathbf{M}_{\mathrm{ECM}} = \begin{bmatrix} 1.000 & 0.0061 & -0.0040 & -0.0004 \\ -0.0004 & 1.0075 & 0.0047 & -0.0025 \\ 0.0048 & -0.0024 & -0.9922 & 0.0091 \\ 0.0024 & -0.0025 & -0.0034 & -1.0010 \end{bmatrix}. \quad \textbf{(17)}$$

Conclusion: In summary, a novel model-free calibration method for DRC-MMP has been proposed. The calibration of the system can be completed only by measuring the polarizers and waveplates of different angles. The entire calibration process does not involve the disassembly and assembly of any system components, and high-precision in-situ calibration can be achieved. There is no need to know the exact parameters of any components in advance or to model the PSG, PSA, and the light source. Therefore, the method is easy, convenient to implement and particularly suitable for the calibration of systems that contain difficult-to-model elements.

Funding. National Natural Science Foundation of China (51775217, 51727809, 52022034); National Major Science and Technology Projects of China (2017ZX02101006-004); Key Research and Development Plan of Hubei Province (2020BAA008).

Disclosures. The authors declare no conflicts of interest.

Data Availability. Data underlying the results presented in this Letter are not publicly available at this time but may be obtained from the authors upon reasonable request.

Supplemental document. See Supplement 1 for supporting content.

REFERENCES

1. Y. Battie, M. Stchakovsky, S. Neveu, D. Jamon, and E. Garcia-Caurel, J. Vac. Sci. Technol. B **37**, 062929 (2019).
2. S. Liu, X. Chen, and C. Zhang, Thin Solid Films **584**, 176 (2015).
3. J. Vizet, J. Rehbinder, S. Deby, S. Roussel, A. Nazac, R. Soufan, C. Genestie, C. Haie-Meder, H. Fernandez, F. Moreau, and A. Pierangelo, Sci. Rep. **7**, 2471 (2017).
4. E. Garcia-Caurel, A. De Martino, and B. Drévillon, Thin Solid Films **455-456**, 120 (2004).
5. R. W. Collins and J. Koh, J. Opt. Soc. Am. A **16**, 1997 (1999).
6. O. Arteaga, M. Baldrís, J. Antó, A. Canillas, E. Pascual, and E. Bertran, Appl. Opt. **53**, 2236 (2014).
7. C. Chen, X. Chen, H. Gu, H. Jiang, C. Zhang, and S. Liu, Meas. Sci. Technol. **30**, 025201 (2019).
8. E. Compain, S. Poirier, and B. Drevillon, Appl. Opt. **38**, 3490 (1999).
9. C. Macías-Romero and P. Török, J. Eur. Opt. Soc. Rap. Public. **7**, 12004 (2012).
10. J. Qi, D. S. Elson, and D. Stoyanov, Opt. Lett. **44**, 2362 (2019).
11. R. Meng, Z. Chen, X. Wang, Y. Liu, H. He, and H. Ma, Appl. Opt. **60**, 1380 (2021).
12. R. Horn and C. Johnson, *Matrix Analysis* (Cambridge University, 1990), Chap. 7.3, pp. 421–425.